



In situ growth of N-doped carbon nanotubes in Fe-Nx/Fe₂O₃/Fe₃O₄-encapsulated carbon sheets for efficient bifunctional oxygen catalysis

Ruihui Gan^a, Yan Song^b, Chang Ma^{a,b,*}, Jingli Shi^{a,**}

^a Tianjin Municipal Key Lab of Advanced Fiber and Energy Storage Technology, Tiangong University, Tianjin 300387, China

^b CAS Key Laboratory of Carbon Materials, Institute of Coal Chemistry, Chinese Academy of Sciences, Taiyuan 030001, China

ARTICLE INFO

Keywords:

Oxygen Catalysis
Composite catalysts
Functionalization
Bifunctional
N-doped Carbon Nanotubes

ABSTRACT

Development of efficient bifunctional oxygen catalysts is of interest for zinc-air batteries (ZABs). However, achieving both highly active and durable oxygen reduction and evolution reactions (ORR/OER) in one catalyst remains challenging. Herein, a composite catalyst (m-Fe/N-C@CNT) integrating N-doped carbon nanotubes (NCNTs) and Fe-Nx/Fe₂O₃/Fe₃O₄-encapsulated carbon nanosheets is obtained by in situ growth and interface induction strategy. SiO₂ is modified with amine groups to anchor Fe³⁺ and inhibit Fe³⁺ reduction, and the resulting Fe₂O₃/Fe₃O₄ nanoparticles convert g-C₃N₄ to NCNTs. m-Fe/N-C@CNT shows superior activity and stability to commercial Pt/C and RuO₂ catalysts in ORR and OER, respectively. The high activity of m-Fe/N-C@CNT is revealed to mainly derive from Fe-Nx moieties, and the contributions of N-C and Fe₂O₃/Fe₃O₄ species are reflected in ORR and OER, respectively. Moreover, the constructed ZABs exhibit a peak power density of 160 mW cm⁻² and recyclability. This work provides a new idea for the preparation of bifunctional oxygen catalysts.

1. Introduction

The massive consumption of fossil fuels has led to a serious energy crisis and environmental pollution in human society, compelling scientists to develop new energy sources that are environmentally friendly, low-cost, and highly efficient [1–4]. Zinc-air batteries (ZABs) have shown great potentials in various candidates due to their ultra-high energy density, zero-emission, and natural resources [5,6]. Oxygen-catalyzed reactions, including oxygen reduction (ORR) and oxygen evolution (OER) reactions, determine the performance of ZABs [6]. However, both ORR and OER suffer from sluggish kinetic processes, which necessitate the application of efficient catalysts during ZABs operation [7,8]. Noble metals and their derivatives are state-of-the-art oxygen catalysts, but their high cost, limited reserves, and monofunctional (Pt for ORR, Ir and Ru for OER) severely hinder the development of ZABs [9–11]. Therefore, it is highly desired to develop cost-effective, earth-abundant, and bifunctional non-noble metals oxygen catalysts.

Atomically dispersed transition metals coordinated with N atoms embedded in carbon (M-N-C, M=Fe, Co, Ni, Mn, Zn, etc.) show great potential for oxygen catalysis [12–16]. Recently, Fe-N-C catalysts have been favored by researchers due to the ultra-high intrinsic activity of

Fe-Nx moieties, which endow the catalysts with optimized adsorption model, d-band shrink, and electron density [17–19]. Commonly, the generated Fe-Nx moieties are buried in micropores, resulting in poor accessibility and remaining inactive [20]. Studies have shown that introducing numerous mesopores to construct reactant transfer channels or directly using mesopores as hosts of Fe-Nx sites would greatly improve accessibility [17,21,22]. Further research also revealed that Fe nanoparticles, such as Fe₂O₃ and Fe₃O₄, could effectively enhance the activity of adjacent Fe-Nx and N-C components via modulating O₂ affinity and reducing energy barriers in rate determining step [23–25]. In the subsequent catalytic process, they synergize and give the target catalysts remarkable catalytic activity.

Normally, oxidation of carbon substrates during catalysis triggers the demetallation of Fe species, then brings about a deterioration in stability [26,27]. Therefore, a highly graphitized carbon substrate exhibiting strong corrosion/oxidation resistance is required. Increasing the metal dosage and raising the pyrolysis temperature are two commonly used ways to enhance the graphitization degree of carbon [28,29]. However, these methods always lead to a decrease in activity due to the collapse of the local carbon structure [30–32]. In situ formation of highly graphitized carbon, such as graphene and carbon nanotubes (CNTs), in a

* Corresponding author at: Tianjin Municipal Key Lab of Advanced Fiber and Energy Storage Technology, Tiangong University, Tianjin 300387, China.

** Corresponding author.

E-mail addresses: fdoy_1t54@163.com (C. Ma), shijingli1963@163.com (J. Shi).

carbon substrate should be a better approach. Graphene/CNTs not only increase the degree of graphitization, but also effectively protect metal nanoparticles from electrolyte leaching and provide additional active sites [14,33,34]. In addition, the high conductivity of graphene/CNTs can eliminate the deactivation caused by hydroxylation of the Fe sites during the OER process [35–37]. However, fabricating such composite catalysts in ZABs through a facile way and achieving efficient oxygen catalysis remains challenging.

Herein, a strategy combining functionalization and in situ engineering is developed to construct a composite electrocatalyst consisting of Fe-Nx/Fe₂O₃/Fe₃O₄-encapsulated porous carbon sheets and N-doped CNTs (m-Fe/N-C@CNT) for robust oxygen catalysis in ZABs. Amine groups (-NH₂) were decorated on the surface of SiO₂ nanoparticles, inducing formation of numerous accessible Fe-Nx moieties on carbon sheets. Fe₂O₃/Fe₃O₄ nanoparticles coexist and are well-protected by graphene/CNTs. Urea was used as a precursor of g-C₃N₄, which was converted to N-doped CNTs under the catalytic effect of Fe₂O₃/Fe₃O₄ nanoparticles, avoiding the use of toxic cyanamide or dicyanamide in convention route. Benefiting from the unique structure, the resulted m-Fe/N-C@CNT exhibits higher activity and stability than the benchmark Pt/C and RuO₂ in ORR and OER, respectively. It is revealed that Fe-Nx moieties contribute significantly to oxygen catalysis of m-Fe/N-C@CNT, while N-C and Fe₂O₃/Fe₃O₄ components further enhance the ORR and OER activities by synergizing with Fe-Nx moieties. The constructed ZABs based on m-Fe/N-C@CNT cathode show a peak power density of 160 mW cm⁻² and excellent recyclability, outperforming than Pt/C+RuO₂ counterparts.

2. Experimental

2.1. The modification of SiO₂

10 g of SiO₂ (particle size: 30 ± 10 nm) nanoparticles were dried at 120 °C for 2 h followed by adding to 350 ml of ethanol and injecting with 3 ml of (3-Aminopropyl)triethoxysilane (APTS) solution. The mixture was refluxed and stirred at 70 °C for 36 h, then washed three times with ethanol and distilled water and dried at 60 °C. Finally, the APTS-modified SiO₂ nanoparticles (m-SiO₂) were obtained.

2.2. Synthesis of m-Fe/N-C@CNT

For m-Fe/N-C@CNT preparation, 0.5 g of m-SiO₂ and 100 mg of FeCl₃ nanoparticles were added to 50 ml of distilled water and sonicated for 10 min. Then, 0.6 g of L-aspartic acid was added to the mixture and stirred at 70 °C for 30 min, completely dried in an oven at 80 °C. The dried powder was then grinded with 6 g of urea in an agate mortar for 30 min, and calcined at 500 and 800 °C for 2 and 1 h, respectively, with a heating rate of 3 °C/min and Ar protection. The obtained carbon was etched with a 10 wt% HF solution for 8 h at room temperature, then rinsed with distilled water and dried at 60 °C. For comparison, p-Fe/N-C@CNT and m-Fe/N-C were also fabricated using the same process, except that the unmodified SiO₂ nanoparticles were used for the former and urea was not added for the latter.

2.3. Synthesis of Fe/N-C, m-N-C, and m-C

Fe/N-C was prepared by the same process as m-Fe/N-C@CNT, except that SiO₂ templates were not added. For m-N-C, the L-aspartic acid-coated m-SiO₂ nanoparticles were grinded with urea, then calcined and leached in the same process as m-Fe/N-C@CNT. As for m-C, the L-aspartic acid-coated m-SiO₂ nanoparticles were calcined and leached under the same conditions as m-N-C.

2.4. Materials characterizations

The scanning electron microscopy (SEM) and transmission electron

microscopy (TEM) images were obtained from Gemini SEM500 and FEI TALOS F200X, respectively. X-ray crystal diffraction (XRD) patterns were recorded on Bruker D8 ADVANCE. The surface elemental composition was characterized by X-ray photoelectron spectra (XPS) on Thermo, ESCALAB 250. Nitrogen adsorption and desorption isotherms were examined by a physical adsorption instrument (BELSORP-Max, Japan). Raman spectrums were recorded from XploRA PLUS. The Fe contents in the catalysts were determined by ICP-MS (Agilent 7700X, America).

2.5. Electrochemical measurements

The catalyst ink was prepared by sonicating a mixture of 5 mg of catalyst, 250 μL of DMF, 250 μL of water, and 50 μL of Nafion solution (5 wt%) for 30 mins. We performed electrochemical tests on CHI 760E with a three-electrode system. For ORR, the ink was uniformly transferred to the glassy carbon electrode (d = 5 mm), yielding a catalyst loading of 0.3 mg cm⁻², which was 0.1 mg cm⁻² for Pt/C. The auxiliary and reference electrodes are graphite rods and Ag/AgCl electrodes (saturated KCl solution), respectively. The recorded potentials were converted to reversible hydrogen electrodes (RHE) by the following equation: $E_{RHE} = E_{Ag/AgCl} + 0.059 \text{ pH} + 0.198$. Linear sweep voltammetry (LSV) was performed on N₂- and O₂-saturated 0.1 M KOH solution with a scan rate of 10 mV s⁻¹. The Tafel slopes were determined by the equation: $\eta = \log j + a$. The accelerating durability test were performed in 0.6–1.0 V with a scan rate of 50 mV s⁻¹. Chronoamperometry was performed at 0.6 V for 30,000 s with a rotation speed of 1600 rpm.

As for OER, the catalyst ink was homogeneously pipetted to 1 × 1 cm² nickel foam, yielding the catalyst loading of 0.5 mg cm⁻². Hg/HgO electrode (1.0 M KOH) served as a reference electrode. The recorded potentials were converted to RHE by the equation: $E_{RHE} = E_{Hg/HgO} + 0.059 \text{ pH} + 0.098$. LSV was performed in O₂-saturated 1.0 M KOH solution with a scan rate of 10 mV s⁻¹ and IR corrected. The ADT was performed in 1.2–1.6 V with a scan rate of 100 mV s⁻¹.

For zinc-air batteries (ZABs) assembly, catalyst ink was obtained by dispersing 5 mg of m-Fe/N-C@CNT or Pt/C+RuO₂ (mass ratio of 1:1) in 350 μL of ethanol and 50 μL of Nafion under 30 mins of sonication. Then, 80 μL of catalyst ink was pipetted and coated on carbon paper with catalyst loading of 1 mg cm⁻² to serve as the cathode. A polished zinc plane served as an anode. The electrolyte was a mixture solution of 6 M KOH and 0.2 M Zn(CH₃COO)₂. Before the tests, the fabricated ZABs were stabilized at room temperature for 1 h. The discharge plots were recorded in CHI 760E, and cycling performance was tested in CT3001A (Wuhan LANHE Instrument Company).

3. Result and discussion

3.1. Morphology and structure

Fig. 1 shows the fabrication procedure of m-Fe/N-C@CNT. The APTS treatments endow the SiO₂ nanoparticles with enriched -NH₂ groups on the surface [38], enabling m-SiO₂ to anchor Fe ions strongly. Then, the Fe ion-anchored m-SiO₂ (m-SiO₂@Fe) was mixed with L-aspartic acid and urea, of which L-aspartic acid acts as carbon and nitrogen precursor and urea was mainly employed to provide g-C₃N₄ [39,40]. The surface-anchored Fe ions benefits to the formation of Fe-Nx moieties on the interface of C/SiO₂. The unique texture would generate numerous accessible active sites after HF washing. In addition, a certain degree of Fe species agglomerated into Fe₂O₃/Fe₃O₄ nanoparticles, which catalyzed the conversion of g-C₃N₄ to N-doped CNTs.

To identify whether the APTS treatment has successfully functionalized SiO₂ nanoparticles with -NH₂ groups, XPS survey was carried out. XPS survey spectra (Fig. S1) reveal the existence of considerable content of N element (2.31 at%) on m-SiO₂ (Table S1). Considering the m-SiO₂ experienced long-time washing using ethanol and distilled water, the N is deemed to originate from -NH₂. To investigate the effect of

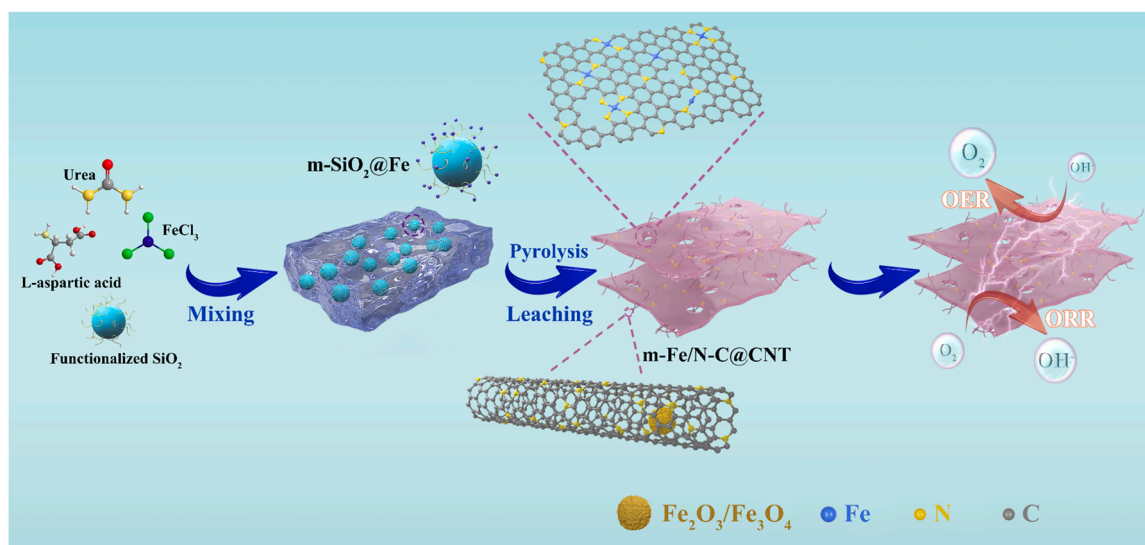


Fig. 1. The fabrication procedure of m-Fe/N-C@CNT.

modification of SiO_2 on the Fe content of the final catalyst, ICP-MS measurement was performed. The results reveal that there are 2.92, and 2.62 wt% Fe element on m-Fe/N-C@CNT and p-Fe/N-C@CNT, respectively, suggesting APTS modification played a positive role in increasing the Fe content. The iron content of m-Fe/N-C (3.69 wt%) is higher than that of m-Fe/N-C@CNT, which should be attributed to Fe ions aggregating into stable Fe nanoparticles in the absence of urea.

The morphology and microstructure of the catalysts were observed with SEM and TEM. From SEM images of m-Fe/N-C@CNT (Fig. 2a, b and

Fig. S2), a composite structure composed of carbon nanosheets and CNTs is widely observed. Such coexistence structure of carbon nanosheet/CNTs also can be clearly found by TEM (Fig. 2c and d). The formation of carbon nanosheets is speculated to be associated with urea. Researches have revealed that urea would be converted into g- C_3N_4 nanosheets by calcination at 550°C [41–43]. With the g- C_3N_4 nanosheets as template, L-aspartic acid evolved into carbon nanosheets during pyrolytic process. At around 700°C , g- C_3N_4 decomposed completely [41], generating numerous stripped carbon nanosheets as

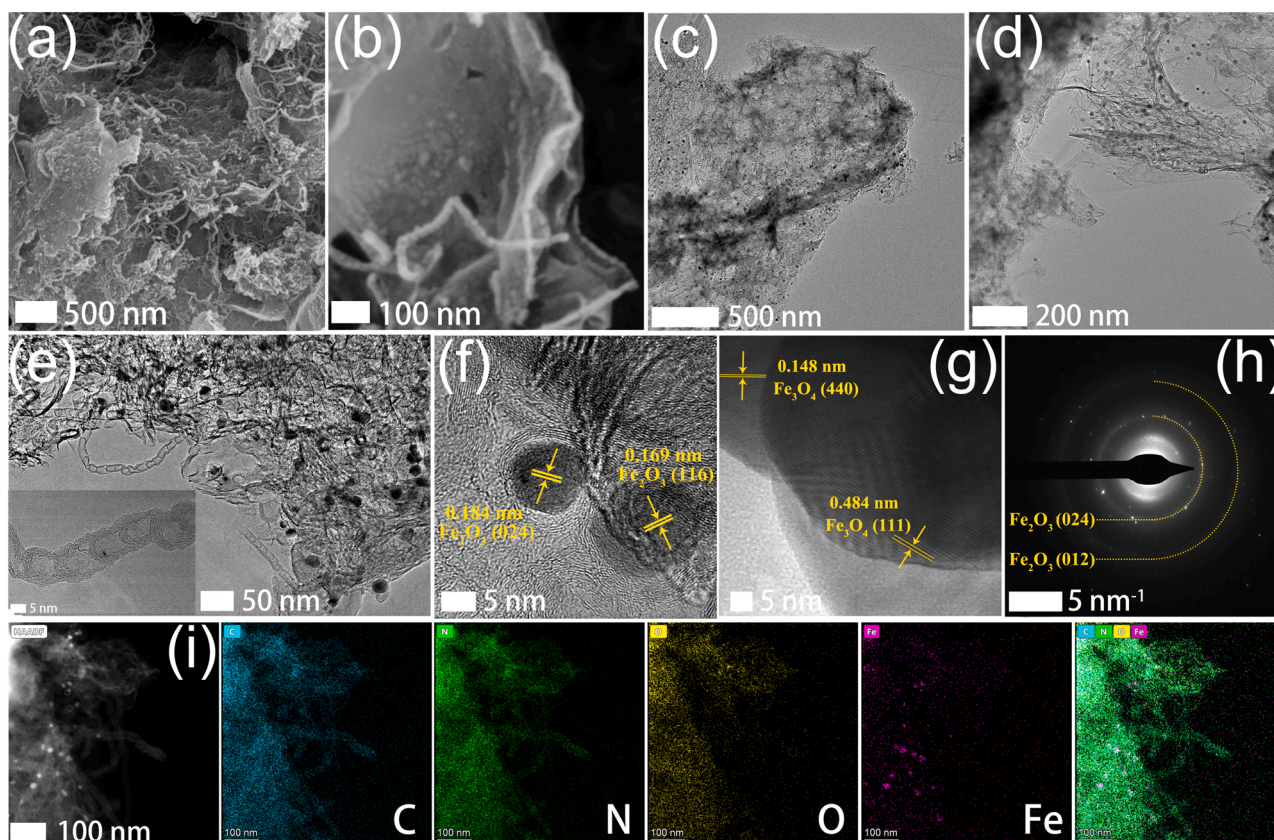


Fig. 2. The morphology analysis of m-Fe/N-C@CNT. (a–b) SEM, (c–e) TEM, (f and g) HR-TEM, (h) SAED, and (i) HAADF-STEM and EDS mapping images (C: cyan, N: green, O: yellow, Fe: purple).

presented in m-Fe/N-C@CNT (Fig. S2).

TEM images in Fig. 2c and d show that numerous tiny nanoparticles are homogeneously dispersed in m-Fe/N-C@CNT, which should be Fe nanoparticles. Clearly, the growth of CNTs is catalyzed by the Fe nanoparticles, of which the mechanism has been unveiled [44]. It is worth noting that p-Fe/N-C@CNT (Fig. S3a-c) displays a higher content of CNTs and Fe nanoparticles than m-Fe/N-C@CNT. It confirms the above conclusion, and suggests that the quantity of CNTs should be related to the number of Fe nanoparticles. Considering the similar synthesis process, the fewer Fe nanoparticles in m-Fe/N-C@CNT should be attributed to the anchoring effect of -NH_2 on Fe^{3+} , which inhibits the formation of Fe nanoparticles.

With Fe nanoparticles, m-Fe/N-C (Fig. S4a-c) does not present both carbon sheets and CNTs, proving an important effect of urea in generating carbon nanosheets and suggesting urea also play a crucial role in growth of CNTs. From enlarged TEM images (Fig. 2d and S3f), it can be observed that CNTs exhibit a typical bamboo-like structure. Such structure has been widely observed in N-doped CNTs [45]. The mapping results (Fig. 2i) also confirm the existence of N in the CNTs. It demonstrates a successful N-doping in CNTs, which has been revealed to enhance conductivity of CNTs [46]. According to the above results, it can be concluded that $\text{g-C}_3\text{N}_4$, derived from urea, provides the major C and N source for growth of CNTs, in agreement with literature [47]. And, it is believed that because of decomposition of $\text{g-C}_3\text{N}_4$, more Fe nanoparticles were exposed, which brought about massive growth of CNTs on m-Fe/N-C@CNT and p-Fe/N-C@CNT. It is worth pointing out that no obvious large-area nanosheets were found in p-Fe/N-C@CNT. It should be attributed to extensive migration and agglomeration of Fe species, which teared the carbon sheets into small fragments as shown in p-Fe/N-C@CNT (Fig. S3).

From HR-TEM images (inset in Fig. 2e and Fig. 2f and g), CNTs are multi-wall CNTs with ca. 8 layers of graphene, and the Fe nanoparticles are wrapped by graphene. It is deduced that it is the graphene layers that effectively protect Fe nanoparticles from HF leaching, and such

protective wrapping would be profited to catalytic stability. The lattice fringes of the nanoparticles are measured to be 0.184, 0.169, 0.148, and 0.484 nm, corresponding to the (024), (116) planes of Fe_2O_3 and the (440), (111) planes of Fe_3O_4 , respectively. In the SAED pattern (Fig. 2h), only the diffraction spots of the (024) and (012) planes of Fe_2O_3 are observed. Hence, it can be concluded that the resultant nanoparticles in m-Fe/N-C@CNT are Fe_2O_3 and Fe_3O_4 , of which the former is dominant.

From the EDS mapping images (Fig. 2i), m-Fe/N-C@CNT contains C, N, O, and Fe elements, the abundant nitrogen is uniformly distributed in both the carbon sheets and CNTs, and the Fe element is mainly distributed in the carbon sheets. Importantly, Fe and N elements are highly overlapped, which implies the formation of Fe-Nx moieties in m-Fe/N-C@CNT.

From Fig. S3h, the Fe nanoparticle of p-Fe/N-C@CNT shows a lattice fringe of 0.169 nm, corresponding to the (116) plane of Fe_2O_3 . For m-Fe/N-C (Fig. S4d-h), the lattice fringe of the nanoparticle is 0.148 nm, corresponding to the (214) plane of Fe_2O_3 . No Fe_3O_4 phase appeared in the TEM images of p-Fe/N-C@CNT and m-Fe/N-C, confirming the dominance of Fe_2O_3 again.

The crystal structure of the samples was investigated using powder XRD. From Fig. 3a, both m-Fe/N-C@CNT and p-Fe/N-C@CNT show only two diffraction peaks of graphitic carbon at ca. 26° and 42° . Besides two weak diffraction peaks of carbon, m-Fe/N-C also displays some sharp diffraction peaks of Fe_2O_3 and Fe_3O_4 phases. Considering the TEM results that all the three samples contain $\text{Fe}_2\text{O}_3/\text{Fe}_3\text{O}_4$ nanoparticles, failure to detect corresponding signal in m-Fe/N-C@CNT and p-Fe/N-C@CNT might be attributed to their smaller particle size, fewer particle quantities, and graphene wrapping. In addition, a clear difference can be observed that p-Fe/N-C@CNT presents a sharper (002) diffraction peak than m-Fe/N-C@CNT. Based on the TEM results, it can be speculated that due to the fixing effect of -NH_2 on Fe, the fewer Fe-related nanoparticles formed, which results into a much lower graphitization degree for m-Fe/N-C@CNT. The Raman patterns (Fig. 3b) show that the I_D/I_G value of m-Fe/N-C@CNT, p-Fe/N-C@CNT, and m-Fe/N-C are 1.04,

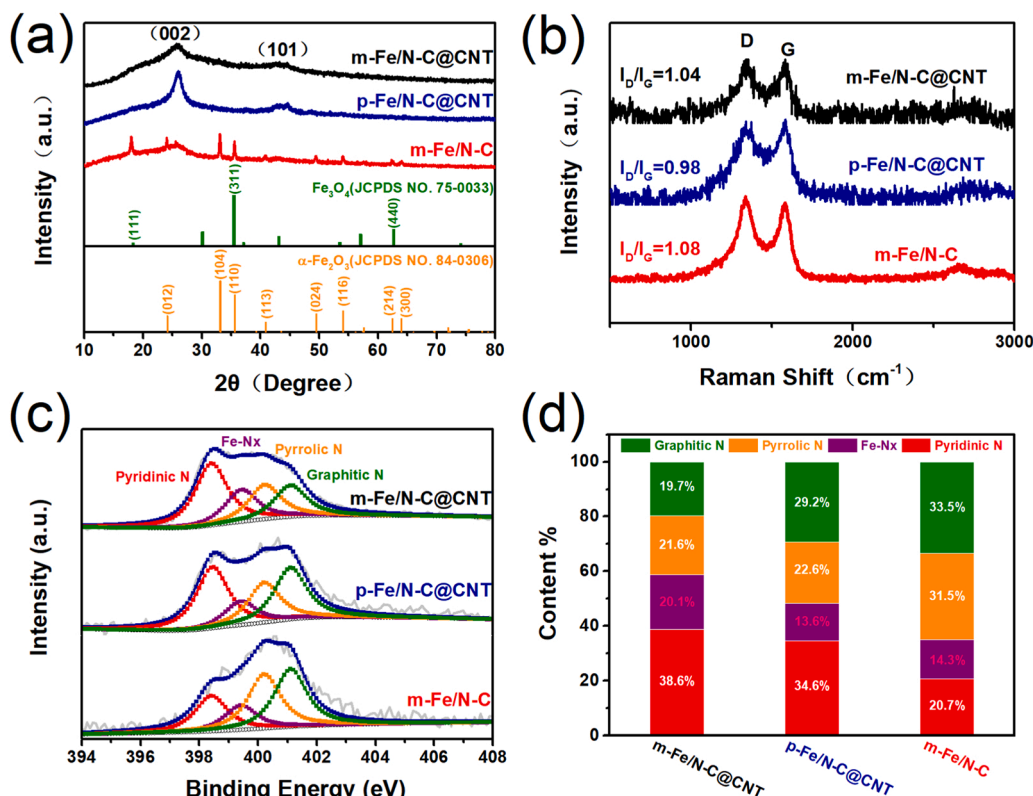


Fig. 3. (a) XRD patterns; (b) Raman patterns; (c) N 1s; and (d) corresponding various N-types content of m-Fe/N-C@CNT, p-Fe/N-C@CNT, and m-Fe/N-C.

0.98, and 1.08, respectively. Being coincident with the XRD results, p-Fe/N-C@CNT has higher graphitization degree than m-Fe/N-C@CNT, while m-Fe/N-C presents the lowest graphitization degree.

To clarify the influence of HF washing on Fe₂O₃/Fe₃O₄ in the catalysts, XRD tests were performed on the samples before washing (Fig. S5). The unwashed Fe/N-C without adding SiO₂ presents strong diffraction peaks of Fe₃O₄ and weak diffraction peaks of Fe₂O₃, indicating a low content of Fe₂O₃. With the introduction of SiO₂, unwashed m-Fe/N-C displays the diffraction peaks of Fe₂O₃ and Fe₃O₄, both of which show much the same intensity. It implies a significant increase of Fe₂O₃ content with the addition of SiO₂. It is speculated that SiO₂, with abundant oxygen functional groups and close to Fe atoms, inhibited the reduction of Fe³⁺ into Fe²⁺ during calcination. It is worth mentioning that all the unwashed samples present diffraction peaks of Fe₃O₄, which show significantly decrease in intensity or disappear after HF-washing. It can be concluded that Fe₃O₄ nanoparticles were greatly removed by HF solution, leaving Fe₂O₃ as dominant phase.

XPS patterns in Fig. S1 show that all three samples contain C, N, and O elements, and only m-Fe/N-C displays Fe signals due to its high Fe content, which is in good agreement with the ICP-MS and XRD results. Table S1 shows the content of the various elements in the catalysts. m-Fe/N-C displays a Fe content of 0.18 at%, which is significantly lower than the value from ICP-MS, probably due to the wrapping of graphene layers. The N content are 10.60, 7.29, and 2.70 at% for m-Fe/N-C@CNT, p-Fe/N-C@CNT, and m-Fe/N-C, respectively.

p-Fe/N-C@CNT, and m-Fe/N-C, respectively. Apparently, calcination with urea effectively increases the N content, which is beneficial to interact with Fe to form Fe-N_x sites. m-Fe/N-C@CNT possesses more N content than p-Fe/N-C@CNT, which implies that single-atom Fe plays a certain role in N fixation. The high-resolution N 1s in Fig. 3c shows that all the samples contain pyridinic N, Fe-N_x moieties, pyrrolic N, and graphitic N, which are located at 398.4, 399.4, 400.2, and 401.1 eV, respectively. From the content of various N-containing species (Fig. 3d), it can be found that the introduction of urea effectively promotes the formation of pyridinic N. The percentages of Fe-N_x moieties in m-Fe/N-C@CNT, p-Fe/N-C@CNT, and m-Fe/N-C are 20.1%, 13.6%, and 14.3%, respectively, demonstrating that the APTS modification facilitates the formation of Fe-N_x moieties. In addition, the larger binding energy shift of N and O in m-Fe/N-C@CNT suggests that the Fe species have stronger electronic effects with neighboring carbon (Fig. S6), which is beneficial to activate the oxygen reactants for a fast four-electron process [48].

N₂ adsorption-desorption isotherms (Fig. S7a, c, e) exhibit both type I and type IV hysteresis loop, revealing the coexistence of micropores and mesopores in the catalysts. The specific surface area (SSA) of m-Fe/N-C@CNT, p-Fe/N-C@CNT, and m-Fe/N-C are 531, 528, and 588 m² g⁻¹, respectively. Pore size distribution (PSD) plots (Fig. S7b, d, f) reveal that the three catalysts have similar micropore and mesopore sizes. Notably, the pore volume of m-Fe/N-C@CNT and m-Fe/N-C is higher than p-Fe/N-C@CNT at ca. 23.1 nm, but lower at ca. 36.5 nm. Taking

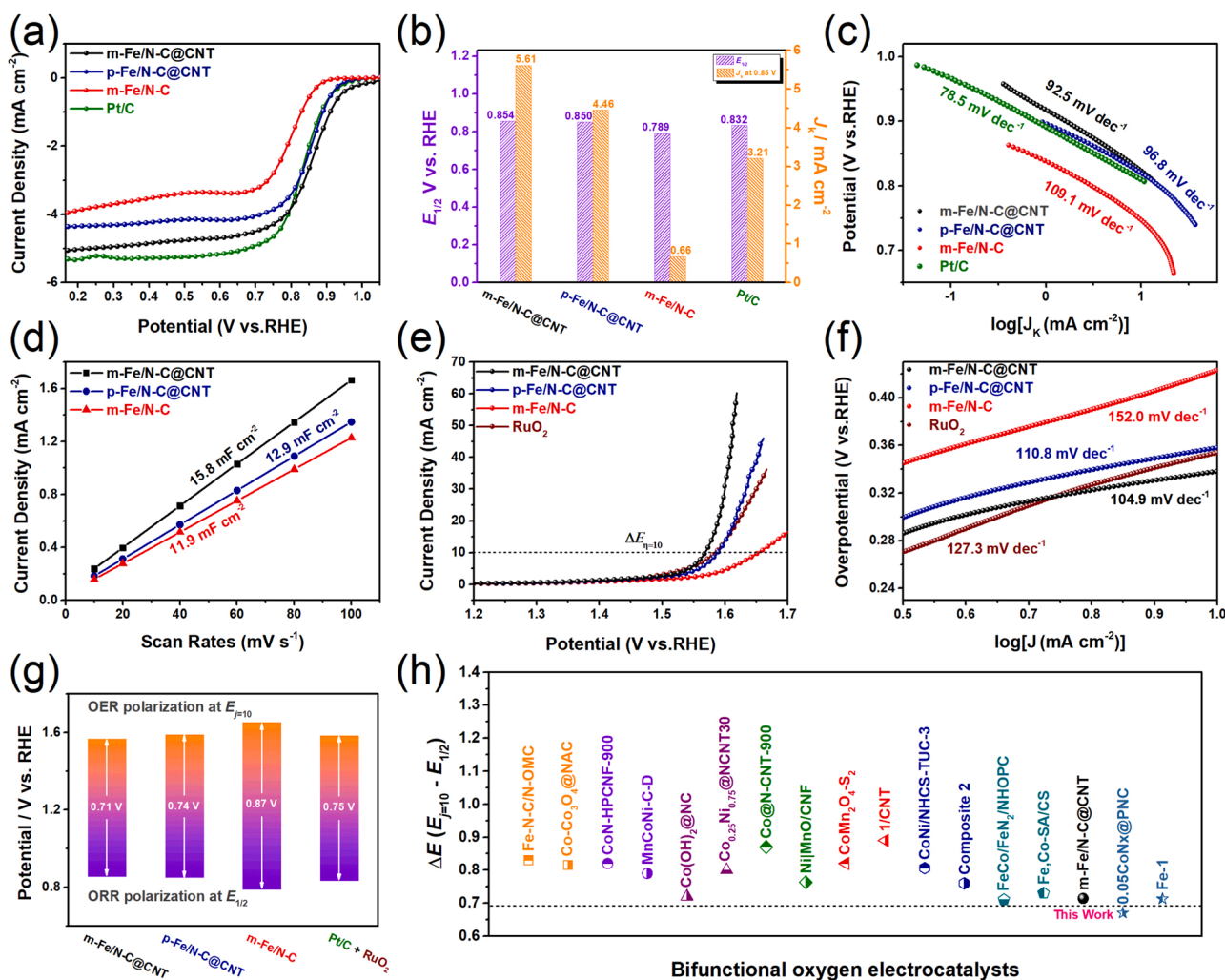


Fig. 4. (a) ORR polarization curves in 0.1 M O₂-saturated KOH solution at 1600 rpm. (b) Corresponding E_{1/2} and J_k at 0.85 V. (c) Tafel slopes for ORR. (d) C_{dl} values. (e) OER polarization curves in 1 M O₂-saturated KOH solution. (f) Tafel slopes for OER. (g) Potential gaps of the as-prepared catalysts and (h) other reported recently transition metal oxygen catalysts.

the ICP-MS results into account, it is inferred that Fe ions are severely agglomerated in p-Fe/N-C@CNT and greatly remove by HF, leaving more mesopores with larger sizes. APTS effectively alleviates the Fe agglomeration in m-Fe/N-C@CNT and m-Fe/N-C due to strong interactions between $-NH_2$ and Fe^{3+} . It is worth mentioning that the similar SSA and PSD can exclude the influence of mass transfer during the catalytic process, allowing for a better understanding of the catalytic mechanism.

3.2. Electrochemical performance

We then evaluated the ORR and OER activities of the as-prepared catalysts in O_2 -saturated KOH solution (0.1 M for ORR and 1 M for OER), with the commercial Pt/C and RuO_2 as the ORR and OER benchmarks, respectively. From ORR polarization curves (Fig. 4a), m-Fe/N-C@CNT shows the impressive ORR activity with onset potential (E_0), half-wave potential ($E_{1/2}$), and limiting current density (J_L) of 1.036 V, 0.854 V, and 5.04 mA cm^{-2} , respectively. The ORR activity of m-Fe/N-C@CNT is superior to benchmark Pt/C ($E_0 = 0.967 \text{ V}$, $E_{1/2} = 0.832 \text{ V}$, $J_L = 5.30 \text{ mA cm}^{-2}$), p-Fe/N-C@CNT ($E_0 = 0.954 \text{ V}$, $E_{1/2} = 0.850 \text{ V}$, $J_L = 4.36 \text{ mA cm}^{-2}$), and m-Fe/N-C ($E_0 = 0.893 \text{ V}$, $E_{1/2} = 0.789 \text{ V}$, $J_L = 3.96 \text{ mA cm}^{-2}$) (Fig. 4a, b). m-Fe/N-C with numerous Fe_2O_3/Fe_3O_4 nanoparticles shows an inferior ORR activity, indicating a limited contribution of sole Fe_2O_3/Fe_3O_4 nanoparticles in ORR. In contrast, m-Fe/N-C@CNT and p-Fe/N-C@CNT display significantly-improved ORR activity at relatively low content of Fe_2O_3/Fe_3O_4 nanoparticles. This demonstrates that calcination with urea plays a crucial role in enhancing ORR activity via introducing Fe-Nx and N-C species. m-Fe/N-C@CNT with more Fe-Nx and N-C species delivers a superior E_0 and J_L to p-Fe/N-C@CNT. Considering a limited difference in the content of N-C species between m-Fe/N-C@CNT and p-Fe/N-C@CNT, the greatly-enhanced ORR activity of m-Fe/N-C@CNT should be mainly due to Fe-Nx species. It is worth emphasizing that it is the APTS functionalization that increases the density of Fe-Nx sites via fixing the Fe ions with $-NH_2$ groups. Nyquist plots in Fig. S8 show that m-Fe/N-C@CNT and p-Fe/N-C@CNT have similar charge transfer resistances, which are much lower than that of m-Fe/N-C. Obviously, it should be mainly attributed to the rich and highly-dispersed CNTs. Also, it is reasonable to believe that by virtue of the abundant active sites and the fast electron transport provided by CNTs, m-Fe/N-C@CNT shows the highest kinetic current density of 5.61 mA cm^{-2} at 0.85 V, far superior to that of p-Fe/N-C@CNT (4.46 mA cm^{-2}), m-Fe/N-C (0.66 mA cm^{-2}), and Pt/C (3.21 mA cm^{-2}). The Tafel slopes of m-Fe/N-C@CNT is 92.5 mV dec^{-1} , which is close to Pt/C (78.5 mV dec^{-1}) but lower than p-Fe/N-C@CNT (96.8 mV dec^{-1}) and m-Fe/N-C ($109.1 \text{ mV dec}^{-1}$), revealing a fast kinetic process. From K-L plots in Fig. S9, m-Fe/N-C@CNT displays an electron transfer number of 3.52, higher than p-Fe/N-C@CNT (2.92) and m-Fe/N-C (2.59). CV test was performed at non-Faradic regions with various scan rates to obtain C_{dl} values of each sample (Fig. S10 and Fig. 4d). The double-layer capacitance (C_{dl}) value of m-Fe/N-C@CNT is 15.8 mF cm^{-2} , which is higher than p-Fe/N-C@CNT (12.9 mF cm^{-2}) and m-Fe/N-C (11.9 mF cm^{-2}). The highest C_{dl} value of m-Fe/N-C@CNT reveals the largest electrochemical surface area, namely, m-Fe/N-C@CNT has the most accessible active sites among three catalysts.

For OER, the overpotential ($\eta_{10} = E_{j=10} - 1.23 \text{ V}$) of m-Fe/N-C@CNT is 338 mV, which is lower than that of p-Fe/N-C@CNT ($\eta_{10} = 358 \text{ mV}$), m-Fe/N-C ($\eta_{10} = 423 \text{ mV}$), and benchmark RuO_2 ($\eta_{10} = 354 \text{ mV}$) (Fig. 4e). Relying on the abundant Fe-Nx, N-C, and Fe_2O_3/Fe_3O_4 species and high conductivity, m-Fe/N-C@CNT possesses better OER activity than p-Fe/N-C@CNT and m-Fe/N-C, and even outperforms the commercial RuO_2 catalyst. The OER Tafel slope (Fig. 4f) of m-Fe/N-C@CNT is $104.9 \text{ mV dec}^{-1}$, which is lower than p-Fe/N-C@CNT ($110.8 \text{ mV dec}^{-1}$), m-Fe/N-C ($152.0 \text{ mV dec}^{-1}$), and RuO_2 ($127.3 \text{ mV dec}^{-1}$). m-Fe/N-C@CNT exhibits a rapid kinetic process even under harsh OER conditions. In general, the gap between $E_{1/2}$ in the ORR and $E_{j=10}$ in the OER ($\Delta E = E_{j=10} - E_{1/2}$) is used to evaluate the bifunctional activity of

the catalyst. Intriguingly, m-Fe/N-C@CNT shows a small ΔE value of 0.71 V, lower than p-Fe/N-C@CNT ($\Delta E = 0.74 \text{ V}$), m-Fe/N-C ($\Delta E = 0.87 \text{ V}$), and noble commercial catalyst Pt/C + RuO_2 ($\Delta E = 0.75 \text{ V}$) (Fig. 4g), showing an extraordinary bifunctional activity. Importantly, the bifunctionality of the as-prepared m-Fe/N-C@CNT is also superior to most non-noble precious metal catalysts reported recently (Fig. 4h and Table S2). Such outstanding bifunctionality should be due to the unique configuration, of which abundant Fe-Nx and N-C species provide high-concentration and high-activity sites towards both ORR and OER, Fe_2O_3/Fe_3O_4 nanoparticles wrapped in few-layer graphene further enhance the activity of adjacent sites, and numerous high-dispersed CNTs construct a highly-conductive skeleton.

In order to clarify the origin of the high bifunctional activity of m-Fe/N-C@CNT, comparative samples of Fe-free (named m-N-C) and Fe-, N-free (named m-C) were prepared and tested for their ORR and OER activities. From polarization curves (Fig. 5a), m-C ($E_0 = 0.880 \text{ V}$, $E_{1/2} = 0.777 \text{ V}$, $J_L = 3.76 \text{ mA cm}^{-2}$) shows the worst ORR activity, indicating that the integration of Fe_2O_3/Fe_3O_4 nanoparticles into carbon slightly improves the ORR activity of m-Fe/N-C. On the contrary, the high ORR activity of m-N-C ($E_0 = 0.939 \text{ V}$, $E_{1/2} = 0.845 \text{ V}$, $J_L = 3.95 \text{ mA cm}^{-2}$) suggests that the contribution of N-C active sites cannot be ignored in m-Fe/N-C@CNT. From Fig. 5b, both m-N-C ($\eta_{10} = 409 \text{ mV}$) and m-C ($\eta_{10} = 437 \text{ mV}$) exhibit inferior OER activity, indicating that N-C active sites play a limited role during OER. The better ORR and OER activity and higher current density of m-Fe/N-C@CNTs highlight the superiority of Fe-Nx species and CNTs in oxygen catalysis. Furthermore, it can be concluded that the high ORR and OER activities of m-Fe/N-C@CNT originate from Fe-Nx, N-C, and Fe_2O_3/Fe_3O_4 species. To clearly identify the contribution of each active component in the ORR process, LSV was performed in O_2 -saturated 0.1 M KOH solution that contained 2 mM $K_3[Fe(CN)_6]$. The $[Fe(CN)_6]^{3-}$ can bind strongly with the Fe sites and cause their inactivation, but cannot affect the activity of the N-C sites. Since the graphene layers protect Fe_2O_3/Fe_3O_4 nanoparticles in m-Fe/N-C@CNT, $[Fe(CN)_6]^{3-}$ only poisons the Fe-Nx sites. Fig. 5c shows that the E_0 and $E_{1/2}$ of m-Fe/N-C@CNT negatively shift to 0.925 and 0.807 V in the presence of $K_3[Fe(CN)_6]$, respectively. Compared with the pristine m-Fe/N-C@CNT, there is a significant attenuation of the performance after poisoning, where E_0 and $E_{1/2}$ are negatively shifted by 111 and 47 mV, respectively. The decay of m-Fe/N-C@CNT in ORR reveals that Fe-Nx species are the major active component. To investigate the role of Fe_2O_3/Fe_3O_4 nanoparticles in the catalytic process of m-Fe/N-C@CNT, m-Fe/N-C@CNT was rinsed with H_2SO_4 for 8 h. From Fig. 5d, e, m-Fe/N-C@CNT presents E_0 of 0.956 V, $E_{1/2}$ of 0.842 V, J_L of 4.86 mA cm^{-2} , and η_{10} of 359 mV. After H_2SO_4 pickling, the $E_{1/2}$ and η_{10} of m-Fe/N-C@CNT loses 12 and 21 mV, respectively. Considering the H_2SO_4 pickling only removed the Fe_2O_3/Fe_3O_4 nanoparticles, it can be inferred that the lost activity of m-Fe/N-C@CNT should be associated with Fe_2O_3/Fe_3O_4 nanoparticles. The results demonstrate that Fe_2O_3/Fe_3O_4 nanoparticles play an active role in both OER and ORR, and the contribution for OER is more remarkable than that for ORR. Comparing Figs. 5c and 5d, one can conclude that Fe-Nx species contributes more than Fe_2O_3/Fe_3O_4 nanoparticles in catalyzing ORR. Fig. 5f proposes a possible catalytic mechanism of m-Fe/N-C@CNT for oxygen catalysis. The electrons transferred to Fe-Nx and N-C sites rapidly through CNTs for efficient ORR and OER catalysis, while Fe_2O_3/Fe_3O_4 nanoparticles further improve catalytic performance by enhancing the activity of adjacent Fe-Nx and N-C species.

The durability of m-Fe/N-C@CNT was also evaluated in ORR and OER via accelerating durability test (ADT). Fig. 6a shows the activity decay of m-Fe/N-C@CNT before and after 8000 cycles during ORR. The $E_{1/2}$ of m-Fe/N-C@CNT shifted negatively by 13 mV after 8000 cycles, while that of Pt/C shifted negatively by 12 mV (inset in Fig. 6a). The decay of m-Fe/N-C@CNT and Pt/C after ADT shows no obvious difference, for which the chronoamperometry was performed. After 30,000 s, the current retention of m-Fe/N-C@CNT is 88% while that of Pt/C is 82% (Fig. 6b), demonstrating m-Fe/N-C@CNT possesses better

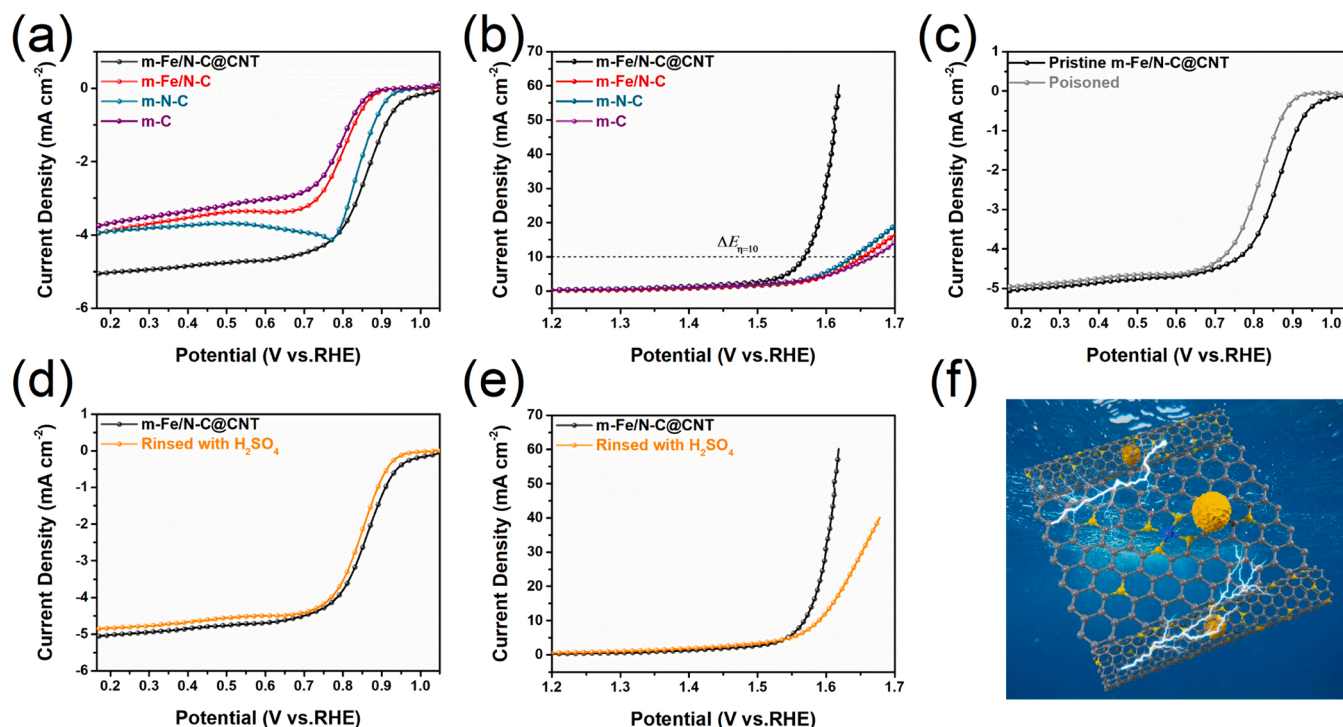


Fig. 5. ORR (a) and OER (b) polarization curves of m-Fe/N-C@CNT, m-Fe/N-C, m-N-C, and m-C, respectively. (c) ORR polarization curves of m-Fe/N-C@CNT in O₂-saturated 0.1 M KOH solution without and in the presence of 2 mM K₃[Fe(CN)₆]. (d, e) ORR and OER polarization curves of m-Fe/N-C@CNT before and after 0.5 M H₂SO₄ rinsed, respectively. (f) Catalytic Mechanism of m-Fe/N-C@CNT.

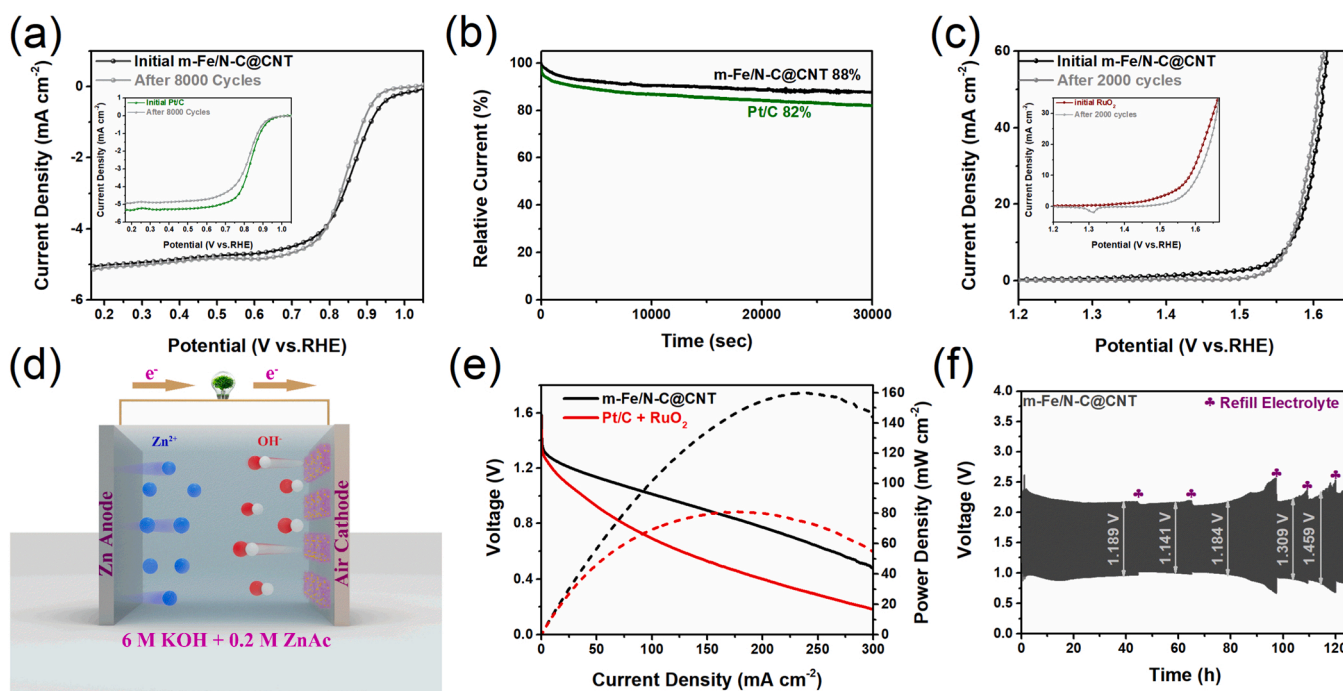


Fig. 6. (a) ADT plots of m-Fe/N-C@CNT and Pt/C (inset). (b) I-t curves of m-Fe/N-C@CNT and Pt/C. (c) ADT plots of m-Fe/N-C@CNT and RuO₂ (inset). (d) Diagram of the ZABs. (e) Polarization and power density curves of m-Fe/N-C@CNT and Pt/C + RuO₂-based ZABs. (f) Charge-discharge plots of m-Fe/N-C@CNT.

durability than Pt/C in ORR. For OER durability, the η_{10} of m-Fe/N-C@CNT did not decay after 2000 cycles, while the η_{10} of RuO₂ increased from 354 mV to 376 mV (Fig. 6c and inset). m-Fe/N-C@CNT shows favorable durability even under harsh OER conditions, outperforming the benchmark RuO₂. The results of ADT show that m-Fe/N-C@CNT possess a well tolerance resistance in alkaline conditions. ZABs were

constructed for evaluate practical application effect of the m-Fe/N-C@CNT catalyst, and Pt/C+RuO₂-based ZABs were used for comparative study (Fig. 6d). Fig. 6e shows that m-Fe/N-C@CNT-based ZABs exhibits smoother discharge process and higher peak power density (160 mW cm⁻²) than Pt/C+RuO₂-based ZABs (81 mW cm⁻²). Fig. 6f shows that m-Fe/N-C@CNT-based ZABs exhibit small charge-discharge

potential gaps and maintain a good performance after several electrolyte refills, exhibiting an excellent cycling stability. With efficient and stable bifunctional oxygen catalytic activity, simple synthesis process and low cost, the as-prepared m-Fe/N-C@CNTs catalyst holds great potential to replace noble metal catalysts for ZABs.

4. Conclusion

In summary, we innovatively combined functionalization and in situ engineering to prepare a composite catalyst integrating N-doped CNTs and Fe-Nx/Fe₂O₃/Fe₃O₄-encapsulated carbon sheets. The -NH₂ grafted on the SiO₂ surface confined Fe³⁺ ions at high temperature and generated a high density of accessible Fe-Nx moieties. Abundant oxygen group of SiO₂ restrained the reduction of Fe³⁺ ions and allowed the coexistence of Fe₂O₃ and Fe₃O₄ nanoparticles. Urea was converted to highly-dispersed N-doped CNTs under the catalytic effect of Fe₂O₃/Fe₃O₄ nanoparticles and provided extra N-C sites. Attributed to these, m-Fe/N-C@CNT showed a $E_{1/2}$ of 0.854 V and a η_{10} of 338 mV, superior to commercial Pt/C and RuO₂ in ORR and OER, respectively. The high activity for both ORR and OER has been revealed to mainly derived from Fe-Nx moieties, and N-C species played a nonnegligible role while Fe₂O₃/Fe₃O₄ nanoparticles further improve catalytic performance by enhancing the activity of adjacent Fe-Nx and N-C species. m-Fe/N-C@CNT showed remarkable stability under the protection of graphene/CNTs. The constructed ZABs based on m-Fe/N-C@CNT cathode showed a peak power density of 160 W cm⁻² and well recyclability. This work provides a feasible route for the preparation of highly efficient bifunctional oxygen catalysts to replace noble metal catalysts in practical applications.

CRediT authorship contribution statement

Ruihui Gan: Conceptualization, Formal analysis, Data curation, Investigation, Writing – original draft. **Yan Song:** Writing – review & editing. **Chang Ma:** Writing – review & editing, Project administration, Funding acquisition. **Jingli Shi:** Supervision, Funding acquisition.

Declaration of Competing Interest

The authors declare that they have no known competing financial interests or personal relationships that could have appeared to influence the work reported in this paper.

Data Availability

Data will be made available on request.

Acknowledgments

The authors acknowledge financial support from the National Key Research and Development Project (No. 2017YFB0308200) and the CAS Key Laboratory of Carbon Materials (KLCMKFJJ2011). We would like to thank the Analytical & Testing Center of Tiangong University for structured illumination microscopy work.

Appendix A. Supporting information

Supplementary data associated with this article can be found in the online version at [doi:10.1016/j.apcatb.2023.122443](https://doi.org/10.1016/j.apcatb.2023.122443).

References

- [1] X. Liu, S. Hao, G. Zheng, Z. Su, Y. Wang, Q. Wang, L. Lei, Y. He, X. Zhang, *J. Energy Chem.* 64 (2022) 315–322.
- [2] T. Lazaridis, B.M. Stühmeier, H.A. Gasteiger, H.A. El-Sayed, *Nat. Catal.* 5 (2022) 363–373.
- [3] S. Govindaraju, S.K. Arumugasamy, G. Chellasamy, K. Yun, J. Hazard. Mater. 421 (2022), 126720.
- [4] H. Yang, X. Wang, T. Zheng, N.C. Cuello, G. Goenaga, T.A. Zawodzinski, H. Tian, J. T. Wright, R.W. Meulenberg, X. Wang, Z. Xia, S. Ma, C.C.S. Chemistry 3 (2021) 208–218.
- [5] Z. Zhang, H. Sun, J. Li, Z. Shi, M. Fan, H. Bian, T. Wang, D. Gao, J. Power, Sources 491 (2021), 229584.
- [6] X. Wang, R.K.M. Raghupathy, C.J. Querebillo, Z. Liao, D. Li, K. Lin, M. Hantusch, Z. Sofer, B. Li, E. Zschech, I.M. Weidinger, T.D. Kuhne, H. Mirhosseini, M. Yu, X. Feng, *Adv. Mater.* 33 (2021), 2008752.
- [7] C.X. Zhao, J.N. Liu, B.Q. Li, D. Ren, X. Chen, J. Yu, Q. Zhang, *Adv. Funct. Mater.* 30 (2020), 2003619.
- [8] P. Zhang, T. Zhan, H. Rong, Y. Feng, Y. Wen, J. Zhao, L. Wang, X. Liu, W. Hou, *J. Colloid Interf. Sci.* 579 (2020) 1–11.
- [9] Y. Zhang, T. Lu, Y. Ye, W. Dai, Y. Zhu, Y. Pan, *ACS Appl. Mater. Inter.* 12 (2020) 32548–32555.
- [10] N.F. Yu, C. Wu, W. Huang, Y.H. Chen, D.Q. Ruan, K.L. Bao, H. Chen, Y. Zhang, Y. Zhu, Q.H. Huang, W.H. Lai, Y.X. Wang, H.G. Liao, S.G. Sun, Y.P. Wu, J. Wang, *Nano Energy* 77 (2020), 105200.
- [11] M.Y. Ye, S. Li, X. Zhao, N.V. Tarakina, C. Teutloff, W.Y. Chow, R. Bittl, A. Thomas, *Adv. Mater.* 32 (2020), e1903942.
- [12] J. Li, M. Chen, D.A. Cullen, S. Hwang, M. Wang, B. Li, K. Liu, S. Karakalos, M. Lucero, H. Zhang, C. Lei, H. Xu, G.E. Sterbinsky, Z. Feng, D. Su, K.L. More, G. Wang, Z. Wang, *G. Wu, Nat. Catal.* 1 (2018) 935–945.
- [13] H. Su, X. Zhao, W. Cheng, H. Zhang, Y. Li, W. Zhou, M. Liu, Q. Liu, *ACS Energy Lett.* 4 (2019) 1816–1822.
- [14] L. Yan, Y. Xu, P. Chen, S. Zhang, H. Jiang, L. Yang, Y. Wang, L. Zhang, J. Shen, X. Zhao, L. Wang, *Adv. Mater.* 32 (2020), 2003313.
- [15] Y. Chen, S. Ji, Y. Wang, J. Dong, W. Chen, Z. Li, R. Shen, L. Zheng, Z. Zhuang, D. Wang, Y. Li, *Angew. Chem. Int. Ed.* 56 (2017) 6937–6941.
- [16] J. Wang, H. Li, S. Liu, Y. Hu, J. Zhang, M. Xia, Y. Hou, J. Tse, J. Zhang, Y. Zhao, *Angew. Chem. Int. Ed.* 60 (2021) 181–185.
- [17] J. Han, H. Bao, J.Q. Wang, L. Zheng, S. Sun, Z.L. Wang, C. Sun, *Appl. Catal. B-Environ.* 280 (2021), 119411.
- [18] L. Jiao, J. Li, L.L. Richard, Q. Sun, T. Stracensky, E. Liu, M.T. Sougrati, Z. Zhao, F. Yang, S. Zhong, H. Xu, S. Mukerjee, Y. Huang, D.A. Cullen, J.H. Park, M. Ferrandon, D.J. Myers, F. Jaouen, Q. Jia, *Nat. Mater.* 20 (2021) 1385–1391.
- [19] T. Zhou, Y. Zhou, R. Ma, Q. Liu, Y. Zhu, J. Wang, *J. Mater. Chem. A* 5 (2017), 5553–5558.
- [20] F. Jaouen, M. Lefèvre, J.P. Dodelet, M. Cai, *J. Phys. Chem. B* 110 (2006) 5553–5558.
- [21] J. Pampel, T.P. Feller, *Adv. Energy Mater.* 6 (2016), 1502389.
- [22] X. Wan, X. Liu, Y. Li, R. Yu, L. Zheng, W. Yan, H. Wang, M. Xu, J. Shui, *Nat. Catal.* 2 (2019) 259–268.
- [23] M. Wang, T. Liao, X. Zhang, J. Cao, S. Xu, H. Tang, Y. Wang, *Adv. Mater.* 32 (2020), 2101904.
- [24] Z. Xiao, F. Hou, Y. Li, R. Zhang, G. Shen, L. Wang, X. Zhang, Q. Wang, G. Li, *Chem. Eng. Sci.* 207 (2019) 235–246.
- [25] B. Wang, Y. Ye, L. Xu, Y. Quan, W. Wei, W. Zhu, H. Li, J. Xia, *Adv. Funct. Mater.* 30 (2020), 2005834.
- [26] S. Liu, C. Li, M.J. Zachman, Y. Zeng, H. Yu, B. Li, M. Wang, J. Braaten, J. Liu, H. M. Meyer, M. Lucero, A.J. Kropf, E.E. Alp, Q. Gong, Q. Shi, Z. Feng, H. Xu, G. Wang, D.J. Myers, J. Xie, D.A. Cullen, S. Litster, G. Wu, *Nat. Energy* 7 (2022) 652–663.
- [27] Y. He, H. Guo, S. Hwang, X. Yang, Z. He, J. Braaten, S. Karakalos, W. Shan, M. Wang, H. Zhou, Z. Feng, K.L. More, G. Wang, D. Su, D.A. Cullen, L. Fei, S. Litster, G. Wu, *Adv. Mater.* 32 (2020), 2003577.
- [28] M. Xiao, Z. Xing, Z. Jin, C. Liu, J. Ge, J. Zhu, Y. Wang, X. Zhao, Z. Chen, *Adv. Mater.* 32 (2020), 2004900.
- [29] D.W. Kim, H.S. Kil, J. Kim, I. Mochida, K. Nakabayashi, C.K. Rhee, J. Miyawaki, S. H. Yoon, *Carbon* 121 (2017) 301–308.
- [30] X. Wang, Y. Jia, X. Mao, D. Liu, W. He, J. Li, J. Liu, X. Yan, J. Chen, L. Song, A. Du, X. Yao, *Adv. Mater.* 32 (2020), 2000966.
- [31] R.Q. Zhong, Y.X. Wu, Z.B. Liang, W.H. Guo, C.X. Zhi, C. Qu, S. Gao, B.J. Zhu, H. Zhang, R. Zou, *Carbon* 142 (2019) 115–122.
- [32] M. Liu, L. Kong, X. Wang, J. He, X.H. Bu, *Small* 15 (2019), e1903410.
- [33] K. Sheng, Q. Yi, A.L. Chen, Y. Wang, Y. Yan, H. Nie, X. Zhou, *ACS Appl. Mater. Inter.* 13 (2021) 45394–45405.
- [34] A. Kundu, A. Samanta, C.R. Raj, *ACS Appl. Mater. Inter.* 13 (2021) 30486–30496.
- [35] Y. Wang, M. Qiao, X. Mamat, *Chem. Eng. J.* 402 (2020), 126214.
- [36] M.S. Burke, M.G. Kast, L. Trotochaud, A.M. Smith, S.W. Boettcher, *J. Am. Chem. Soc.* 137 (2015) 3638–3648.
- [37] H. Li, Q. Zhou, F. Liu, W. Zhang, Z. Tan, H. Zhou, Z. Huang, S. Jiao, Y. Kuang, *Appl. Catal. B-Environ.* 255 (2019), 117755.
- [38] Y. Ding, W. Sun, W. Yang, Q. Li, *Appl. Catal. B-Environ.* 203 (2017) 372–380.
- [39] J. Liu, T. Zhang, Z. Wang, G. Dawson, W. Chen, *J. Mater. Chem.* 21 (2011) 14398.
- [40] F. Dong, L. Wu, Y. Sun, M. Fu, Z. Wu, S.C. Lee, *J. Mater. Chem.* 21 (2011) 15171.
- [41] W.J. Ong, L.L. Tan, Y.H. Ng, S.T. Yong, S.P. Chai, *Chem. Rev.* 116 (2016) 7159–7329.
- [42] F. Dong, Z. Zhao, T. Xiong, Z. Ni, W. Zhang, Y. Sun, W.K. Ho, *ACS Appl. Mater. Inter.* 5 (2013) 11392–11401.
- [43] J.H. Zhang, M.J. Wei, Z.W. Wei, M. Pan, C.Y. Su, *ACS Appl. Nano Mater.* 3 (2020) 1010–1018.
- [44] V. Jourdain, C. Bichara, *Carbon* 58 (2013) 2–39.
- [45] X. Zhao, S.C. Abbas, Y. Huang, J. Lv, M. Wu, Y. Wang, *Adv. Mater. Interfaces* 5 (2018), 1701448.

- [46] S.V. Bulyarskiy, D.A. Bogdanova, G.G. Gusarov, A.V. Lakalin, A.A. Pavlov, R. M. Ryazanov, *Diam. Relat. Mater.* 109 (2020), 108042.
- [47] X. Liu, W. Yang, L. Chen, Z. Liu, L. Long, S. Wang, C. Liu, S. Dong, J. Jia, *ACS Appl. Mater. Inter.* 12 (2020) 4463–4472.
- [48] H. Wang, W. Wang, Y.Y. Xu, S. Dong, J. Xiao, F. Wang, H. Liu, B.Y. Xia, *ACS Appl. Mater. Inter.* 9 (2017) 10610–10617.